Journal of Power Sources 596 (2024) 234070

Contents lists available at ScienceDirect

Journal of Power Sources

journal homepage: www.elsevier.com/locate/jpowsour

# Optimising anode supported $BaZr_{1-x}Y_xO_{3-\delta}$ electrolytes for solid oxide fuel cells: Microstructure, phase evolution and residual stresses analysis

Sol Fernández Muñoz [a,b], Ricardo Chacartegui [c,d], María D. Alba [a], Joaquín Ramírez Rico [a,b,*]

[a] Instituto de Ciencia de Materiales de Sevilla, CSIC - Universidad de Sevilla, Avda. Américo Vespucio 49, 41092, Seville, Spain
[b] Dpto. Física de La Materia Condensada, Universidad de Sevilla, Avda. Reina Mercedes SN, 41012, Seville, Spain
[c] Dpto. de Ingeniería Energética, Universidad de Sevilla, Escuela Técnica Superior de Ingeniería, Camino Descubrimientos SN, 41092, Seville, Spain
[d] Universidad de Sevilla, Laboratory of Engineering for Energy and Environmental Sustainability, 41092 Seville, Spain

## HIGHLIGHTS

- Sintering conditions control phase purity and microstructure in PCFC electrolytes.
- Optimum conditions for co-firing half cells were found at 1400 °C for 5h.
- Longer sintering times resulted in increased residual stresses and reduced purity.
- Anode reduction reduces compressive residual stresses in the electrolyte.

## ARTICLE INFO

*Keywords:*
Fuel-cell
Electrolyte
Residual stress
Sintering
Proton conductors

## ABSTRACT

Yttrium-doped $BaZrO_3$ is a promising electrolyte for intermediate-temperature protonic ceramic fuel cells. In the anode-supported configuration, a slurry containing the electrolyte is deposited on the surface of a calcined porous anode and sintered. Differences in sintering behaviour and thermal expansion coefficients for the anode and electrolyte result in elastic residual stresses that can impact the long-term stability of the cell during cyclic operation.

Half-cells using $BaZr_{0.8}Y_{0.2}O_{3-\delta}$ as the electrolyte were fabricated using the solid-state reaction sintering method under various sintering conditions. Comprehensive microstructure and residual stress analyses as a function of processing parameters were performed using two-dimensional X-ray diffraction, Rietveld refinement, and scanning electron microscopy, before and after the half-cells were reduced under hydrogen, giving a complete picture of phase, microstructure, and stress evolution under thermal and reduction cycles like the actual operation of the cell.

Our results reveal that a temperature of 1400 °C and shorter soaking times might be advantageous for obtaining phase-pure and thin yttrium-doped $BaZrO_3$ electrolytes with improved microstructure and the presence of compressive residual stress. These findings offer valuable insights into optimising the fabrication process of $BaZrO_3$-based electrolytes, leading to enhanced performance and long-term stability of anode-supported protonic ceramic fuel cells operating at intermediate temperatures.

## 1. Introduction

Electrochemical energy conversion holds immense promise for facilitating the transition towards sustainable energy sources [1]. Among various fuel cell technologies, ceramic solid oxide fuel cells (SOFCs) offer compelling advantages, including (i) high-power density, (ii) low weight and compactness due to electrolyte and electrodes being solid, (iii) reduced cost with no-noble metal electrodes, and (iv) flexibility to utilise fuels such as $H_2$ and hydrocarbons [1–4]. Proton-conducting perovskite-based fuel cells, also known as protonic ceramic fuel cells (PCFCs), are capable of operation at intermediate temperatures, leading to cost reduction and improved long-term operational stability [5]. However, operating at lower temperatures presents material design challenges like decreased electrolyte conductivity and

* Corresponding author. Instituto de Ciencia de Materiales de Sevilla, CSIC - Universidad de Sevilla, Avda. Américo Vespucio 49, 41092, Seville, Spain.
*E-mail address:* jrr@us.es (J. Ramírez Rico).

https://doi.org/10.1016/j.jpowsour.2024.234070
Received 27 October 2023; Received in revised form 21 December 2023; Accepted 8 January 2024
Available online 20 January 2024
0378-7753/© 2024 The Authors. Published by Elsevier B.V. This is an open access article under the CC BY-NC-ND license (http://creativecommons.org/licenses/by-nc-nd/4.0/).

lower rates of electrocatalytic reactions [6].

In the late 1990s, Kreuer et al. [7,8] introduced yttrium-doped barium zirconate (BZY) as a high proton-conducting material for PCFCs exhibiting superior proton conductivity at temperatures below 700 °C compared to the best oxide ion conductors and with good thermodynamic phase stability [9]. To date, cubic perovskite ($ABO_3$) materials, specifically $BaCeO_3$ and $BaZrO_3$ doped with trivalent cations like Y and Yb have been a focal point for research in the field [10] and are widely studied as PCFC electrolytes. These electrolytes operate at temperatures ranging from 400 to 700 °C, with low energy activation energy requirements and high energy efficiency [11].

The main synthesis processes used to obtain proton-conducting electrolytes are divided into two groups: (i) wet reaction methods such as sol-gel [12], and (ii) a solid-state reaction sintering (SSRS) [13–17] which simplifies the fabrication process and reduces the cost. Processing has an impact on the properties, and therefore it must be optimized to achieve optimal cell performance. In this context, the electrolyte properties play a crucial role, demanding reduced electronic leakage, dense layers, large grain sizes, and controlled electrolyte thickness [11,18]. However, obtaining large grain sizes can be challenging due to large grain boundary energies [13] in many proton-conducting ceramics. Grain growth is influenced by the sintering process, which can be tailored to enhance densification and grain sizes by increasing sintering temperatures, soaking times, and/or the amount of sintering aids. However, increasing soaking times and temperatures can cause a decrease of the conductivity by promoting Ba-loss and the diffusion of sintering additives to the B-sites on the Ba*B*$O_3$ perovskite structure [14,19–22]. A recent work by Duan et al. [15,16,23] utilising the SSRS technique with a small amount of NiO (1 wt%) as a sintering aid, showed promise in fully densifying electrolyte layers at reduced sintering temperatures (≤1450 °C).

Moreover, for successful PCFC development, the electrolyte should exhibit good chemical and mechanical stability under operating conditions. Fuel cells typically have a sandwich-type construction consisting of at least three layers: an anode, a cathode, and an electrolyte. The process of co-sintering and the thermal cycling during operation at elevated temperatures can lead to the appearance of residual stresses on the cell's components due to differences in elastic moduli and thermal expansion coefficients [11,24] leading to cracks, delamination, and/or failure of the full device. Proton conducting ceramics are also affected by chemical expansion caused predominantly by hydration when protonic defects are formed in the oxide [25,26]. The lattice expansion due to hydration increases with increasing dopant concentration as oxygen vacancies are increased. Thus, it is crucial to ensure that each component exhibits similar expansion coefficients in the fuel cell's operating range, and some materials may not be suitable for the long-term performance of the fuel cell [27–29]. These challenges limit the use of PCFC and are the reason why PCFCs lag behind SOFC's performance [23].

In this paper, we investigate the effect of sintering conditions in the fabrication of anode-supported $BaZr_{0.8}Y_{0.2}O_{3-\delta}$ (BZY20) electrolytes for PCFCs. Emphasizing simplicity and cost reduction, we employ the SSRS method for the fabrication of the components using $BaZr_{0.8}Y_{0.2}O_{3-\delta}$ as the base proton conductor material due to its proven performance [12,15,16,19,20] in recent years. The electrolyte, the anode, and their integration are studied in two crucial steps: the co-sintering process and the exposure to a reduction cycle. The study of residual stresses on the electrolyte after integration with the anode is emphasized as it is in this stage of the fabrication process where residual stresses will develop [30]. Through an in-depth analysis of residual stresses, microstructure, and composition after electrolyte sintering and reduction, this study provides valuable insights into optimising the manufacturing pathway for PCFCs.

## 2. Experimental details

### 2.1. Half-cell fabrication

$BaZr_{0.8}Y_{0.2}O_{3-\delta}$ (BZY20) powders were synthesised by solid-state reaction sintering (SSRS) using raw $BaCO_3$, $ZrO_2$, and $Y_2O_3$ powders which were ball-milled with isopropanol using $ZrO_2$ milling media, followed by drying and calcination in air up to 1100 °C at 5 °C·min$^{-1}$ during 10 h [30]. The formation of the desired reacted powder phase was confirmed using x-ray diffraction with Cu Kα radiation (Bruker D8I).

For the anode, a composite powder was prepared by mixing 40 wt% of the reacted perovskite-type powders (BZY20), 60 wt% of NiO, and then adding potato starch as a pore former up to 20 wt% weight of the BZY20 + NiO mixtures [15,16]. The resulting mixture was dry-pressed under ~400 MPa for 2 min in a 13 mm diameter steel die. The resulting pellet was then calcined at 800 °C using a heating/cooling rate of 2 °C·min$^{-1}$ for 4 h to introduce bulk porosity upon starch combustion, and to obtain a porous anode in the green state with a thickness ranging between 1.2 and 1.5 mm.

The electrolyte was prepared by mixing 3 g of the BZY20 reacted powders in a vortex mixer with 1 g of dispersant (20 wt% Solsperse 2800 from Lubrizol dissolved in α-Terpineol) and 0.2 g of binder (5 wt% Butvar B-98 dissolved in α-Terpineol) [15]. Although no NiO was added to this slurry, the NiO in the anode will serve as a source of Ni to improve densification during solid-state reaction sintering (SSRS), as it has been shown that Ni can diffuse a few micrometers from the anode into the electrolyte layer [31,32]. A thin electrolyte layer was manually deposited on one side of the anode green pellet using a brush. The half-cell resulting from the experiment was subjected to sintering at various sintering temperatures and soaking times: (i) 1200 °C for 5 h, (ii) 1200 °C for 10 h, (iii) 1325 °C for 5 h, (iv) 1325 °C for 10 h, (v) 1400 °C for 5 h, and (vi) 1400 °C for 10 h. In all cases, heating/cooling rates of 10 °C·min$^{-1}$ were used.

### 2.2. $H_2$-reduction of the half-cells

The anodes in the half-cells consist of NiO and proton-conducting material post-sintering. A reduction process is necessary to convert NiO to Ni-metal, to render it electronically conductive, as well as to produce additional porosity. Typically, this reduction would occur during the first cell operation cycle when $H_2$ is employed as the fuel in an operational system. To emulate this process, a sintered anode was placed inside a high-temperature chamber of a Bruker D8 ADVANCE diffractometer. The anode was subjected to a flowing gas mixture of 5 wt% $H_2$/Ar while the temperature was increased from room temperature to 600 °C at a heating rate of 10 °C·min$^{-1}$. The reduction reaction was monitored *in situ* to determine the extent of the reduction reaction. During reduction, diffraction patterns were collected every 100 °C up to 600 °C, and then every hour at this temperature, allowing us to track the transition from NiO to Ni-metal throughout the reduction process. Identical experiments were performed in half-cells to track the evolution of the electrolyte layer during reduction of the anode.

### 2.3. Microstructural and structural characterisation

The surfaces of the electrolytes were analysed using scanning electron microscopy (SEM, FEI Teneo). SEM images facilitated assessing grain size variations between the electrolyte and their sintered surfaces, aiding in identifying cracks or defects. From the analysis of around 500 grains using ImageJ, we calculated grain sizes and form factors using lognormal statistics. Energy Dispersive X-ray Spectroscopy (EDS, Ametek EDAX) analysis was performed to verify compositional variations in different grain formations. Ambient X-ray diffraction (XRD) patterns of the sintered electrolytes were acquired using a Bruker D8 Advanced diffractometer with $CuK_\alpha$ radiation in the Bragg-Brentano configuration at room temperature. DIFFRAC. EVA and DIFFRACT. TOPAS software

from Bruker and the ICDD2022 database were used for phase identification and structural parameter determination. The lattice parameter *a* of the BZY20-phase was refined using Le Bail analysis [33], which served to determine the amount of yttrium incorporated in the lattice ($Y_{occ}$) via interpolation from literature data (Fig. S4 in the supplementary information). Fig. S1 of the supplementary material shows how the lattice parameter tendency changes above 20 % of $Y_{occ}$, which may be related to increasing Ba-loss, instead of going on linearly increasing since $Y^{+3}$ radii is slightly larger than $Zr^{+4}$ one [34]. Quantitative-phase analysis was then performed using Rietveld refinement: the parameters to be fitted were 6-coefficient Chebychev background, sample displacement correction, lattice parameter, a Lorentzian broadening term describing crystallite size effects (L), a Gaussian broadening term describing microstrain (G) and scale parameters for $Y_2O_3$ (ICDD database, PDF # 41–1105) and $BaY_2NiO_5$ (ICDD database, PDF # 81–1253). For $BaZr_{0.8}Y_{0.2}O_{3-\delta}$ (ICDD database, PDF # 04-015-2511) the Zr and Y occupancies of the perovskite B-site were fixed using previously determined values for $Y_{occ}$.

### 2.4. Residual stress characterisation

Macroscopic (type I) elastic residual stresses were evaluated using a diffractometer (D8 DISCOVER A25) equipped with a Eulerian cradle and an area detector (Väntec 500), where the half-cells were fixed to the sample stage using double-sided tape on the anode-side and the electrolyte face was irradiated. The presence of this macroscopic stress results in a deformation of the crystal lattice (strain) that manifests as a variation in the interplanar spacings *d* compared to what would be found in the absence of stress ($d_0$). This variation in *d* is observed as a displacement of the Bragg peaks, which occupy positions at 2θ instead of $2\theta_0$. The expression of the elastic strain can be obtained from the differentiated form of Bragg's law assuming small variations of the interplanar spacing Δ*d* (Eq. (1)).

$$\varepsilon \approx \frac{(d-d_0)}{d_0} = \frac{\Delta d}{d_0} \approx -cot\ \theta_0(\theta-\theta_0) \quad (1)$$

As only elastic strain alters the mean lattice spacing, this method is sensitive only to elastic, long range macroscopic stresses [35]. The chosen plane for stress calculation was the (3 1 0) plane (equivalent 2θ-angle 70.534°) due to its high angle and peak shift sensitivity [36,37]. It is important to note that this method probes the projection $\varepsilon_{\psi\varphi}$ of the strain tensor $\varepsilon_{ij}$ along the scattering vector (Eq. (2)), which lies in the diffractometer plane and has direction given as $n_{\psi\varphi} = (sin\ \psi\ cos\ \varphi, sin\ \psi\ sin\ \varphi, cos\ \psi)$ in the sample's coordinate system, described by an azimuthal angle (φ) that indicates the rotation of the sample about its surface normal and a tilt angle (ψ) - in conventional Bragg-Brentano diffraction the scattering vector is perpendicular to the sample and thus $\psi = 0$. By determining the strain projections along different sample orientations, the full strain tensor can be estimated.

Due to the small penetration of X-rays into the sample, the diffracted surface layer is thin enough that there are no normal or shear stresses in the diffracting volume (plane stress condition, $\sigma_{33} = \sigma_{13} = \sigma_{31} = 0$), and the stress tensor only has non-zero components $\sigma_{11}$ and $\sigma_{22}$. The strains were then correlated to stress components assuming an isotropic, homogeneous material (Eq. (3)). While the stress-free spacing $d_0$ is generally unknown, it can be approximated by the lattice spacing measured at $\psi = 0$ ($d_{\varphi 0}$) since generally $E >> (\sigma_1 + \sigma_2)$ [35].

In this study, XRD residual stress measurement was done through the $sin^2\ \psi$-method [36,38,39] that assumes plane stress at the sample surface and is based on the linear relation between *d* and $sin^2\ \psi$ given in equation (Eq. 3). Measurements were conducted by varying the tilt angle from 0° to 60° in increments of 10° and determining the interplanar spacing $d_{\psi\varphi}$, which was then plotted against $\sin^2\psi$. Due to the sample geometry and since BZY possesses a cubic structure, the stress tensor is expected to be equibiaxial ($\sigma_{12} = \sigma_{21} = 0$) in the absence of texture, as was confirmed by performing the same measurements at three azimuthal angles ($\varphi = 0°, 45°, 90°$). Taking these relations into account, the macroscopic strain projections were evaluated in a single exposure using the 2D detector [40] and the stresses calculated using known elastic constants for BZY20 are known: Young's modulus E = 209 GPa and Poisson's ratio $\nu = 0.248$ at 20 °C [41].

$$\varepsilon_{\psi\varphi} = n_{\psi\varphi}\ [\varepsilon_{ij}]\ n_{\psi\varphi} \quad (2)$$

$$\varepsilon_{\psi\varphi} = \frac{d_{\psi\varphi}-d_0}{d_0} = \frac{1+\nu}{E}\left(\sigma_{11}\cos^2\varphi + \sigma_{12}\ sin\ 2\varphi + \sigma_{22}\ sin^2\varphi\right) sin^2\psi - \frac{2\nu}{E}\sigma_{11} \quad (3)$$

## 3. Results and discussion

### 3.1. Structural characterisation and composition

The sintering process plays an important role in the phase formation, densification and, subsequently, the electrical and mechanical properties of the electrolyte.

Fig. 1 shows the XRD patterns of sintered electrolytes under various conditions of sintering temperature (1200, 1325 and 1400 °C) and soaking time (5 h and 10 h). The main reflections belong to the BZY20 as primary phase, along with additional minor reflections corresponding to $BaY_2NiO_5$ and $Y_2O_3$ as residual phases. Upon sintering at 1400 °C for 5 h only a small fraction (<1 wt%) of $Y_2O_3$ is observed. The results of Rietveld refinements of these diffraction patterns (examples in Figs. S2 and S3 of the supplementary information, main results in Fig. 2, additional results in Table S1 reveal the robust BZY20 formation with minimal residual yttria at 1400 °C. Conversely, at temperatures below 1400 °C, impurity phases are found in all samples. The presence of $Y_2O_3$ and $BaY_2NiO_5$ alongside the dominant BZY20 phase may hold implications for future fuel cell performance [13,24,42].

The inclusion of NiO promotes the formation of $BaY_2NiO_5$, acting as a liquid phase that accelerates Zr diffusion, thereby reducing its refractory nature. $BaY_2NiO_5$ tends to aggregate at grain boundaries in the final ceramic product [43]. However, the presence of $BaY_2NiO_5$ as a

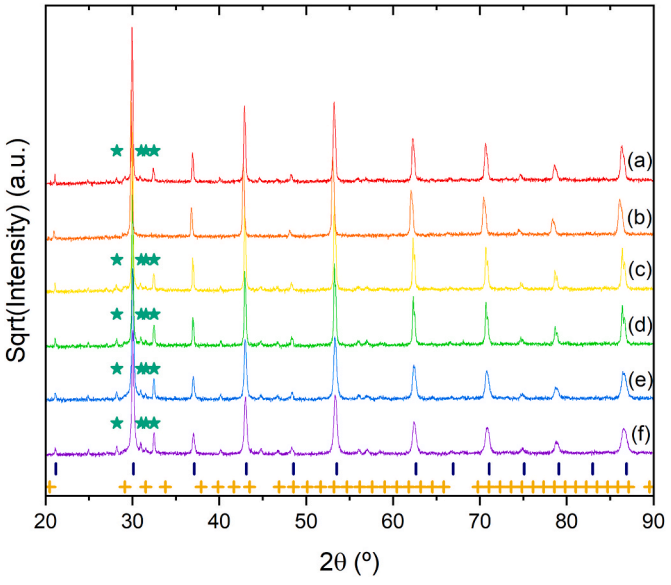


**Fig. 1.** XRD patterns of sintered electrolytes under different conditions:, (a) 1400 °C 10h, (b) 1400 °C 5h, (c) 1325 °C 10h, (d) 1325 °C 5h, (e) 1200 °C 10h, (f) 1200 °C 5h. Sticks (|) indicate the 2θ positions of Bragg reflections for BZY20 (ICDD database, PDF # 04-015-2511). Crosses (+) indicate the 2θ of XRD peaks of $Y_2O_3$ (ICDD database, PDF# 41–1105). Stars (☆) indicate the most significant 2θ of XRD peaks of $BaY_2NiO_5$ according to (ICDD database PDF#81–1253).

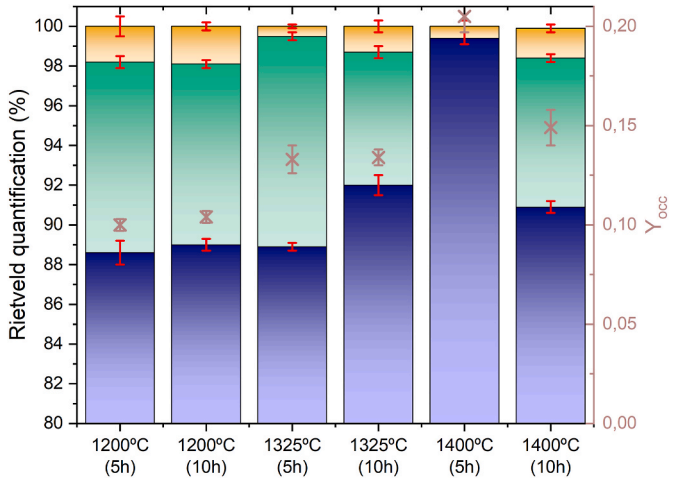


**Fig. 2.** Quantitative phase analysis from Rietveld analysis (Deep blue: BZY20, Aqua: $BaY_2NiO_5$, Gold: $Y_2O_3$) along crosses ( × ) that indicate the Yttrium-occupancy ($Y_{occ}$) in BZY20 structure. $Y_{occ}$ was calculated from the refined lattice parameters by interpolation of literature data. (For interpretation of the references to colour in this figure legend, the reader is referred to the Web version of this article.)

residue results in Ba-deficiency of the primary phase, influencing the incorporation of yttrium within the structure [14,22,43,44]. The relationship between impurity presence, Y-occupancy, and lattice parameter of BZY20-structure at various sintering conditions is shown in Figs. 2 and 3. It is clear that, elevating the sintering temperature enhances yttrium occupancy within the BZY20-structure, subsequently leading to an increase in the lattice parameter [41]. The integration of the dopant is expected to have an influence on proton uptake as it creates vacancies [8,45]. Below 1400 °C, soaking time has no notable impact on reaction. In the case of reaction at 1400 °C, lower soaking times lead to higher Y-substitution (Fig. 3) and the absence of $BaY_2NiO_5$-phase (Fig. 2).

### 3.2. Effect of sintering parameters on the microstructure

Fig. 4 presents representative SEM images showcasing the surface of the sintered electrolyte at temperatures ranging from 1200 °C to 1400 °C for 5 and 10 h. With increasing temperature, grain growth becomes evident at 1325 °C, resulting in homogeneous grains sizes of

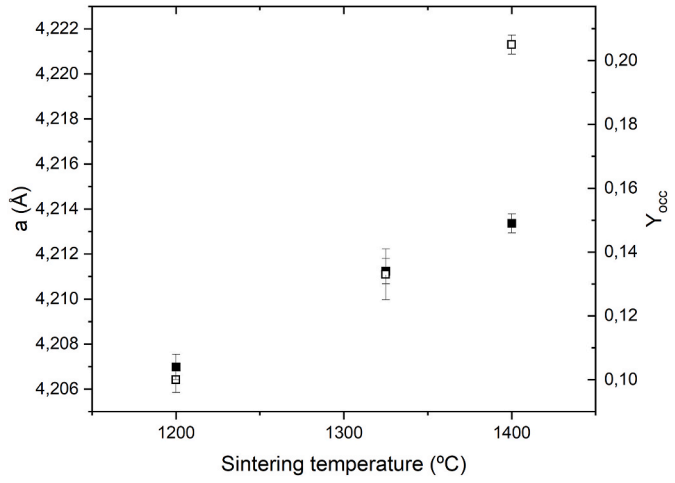


**Fig. 3.** Variation of the lattice parameter and yttrium occupancy of BZY20 at different sintering conditions. Full-square (■) represents the samples that were sintered for 10 h and the blank-square (□) represents the samples that were sintered for 5 h, both with a heating/cooling rate of 10 °C·min$^{-1}$.

approximately 1 μm in size for a sintering temperature of 1400 °C (Table 1). While the impact of soaking time on grain sizes appears less pronounced, elevating the sintering temperature is more effective in promoting grain growth [31]. At 1200 °C samples exhibit smaller, loosely connected grains. Increasing the sintering temperature, at 1325 °C, the grain growth becomes more pronounced, and the grains are interconnected. However, the grains still exhibit relatively small size, which could result in non-favourable electrical conductivity properties due to a larger contribution of grain boundaries. At a sintering temperature of 1400 °C the obtained grain size is the range 1–3 μm as reported in existing literature [15,46,47]. Notably, there is no need to introduce additional NiO in the electrolyte precursor as the NiO diffusing from the anode proves sufficient for promoting densification [14]. Additionally, distinct and larger grains with different morphologies emerge, suggesting the presence of another phase, which was later identified as a $(Ba,Y,Ni)O_x$ and confirmed through EDS to correspond to the $BaY_2NiO_5$ phase previously identified in XRD (Fig. 1). Such impurities are typically observed in Y- and Ni-rich compositions as solidified transient-liquid residual phases [14,24,31]. The formation of impurities, especially Ni-rich areas, could lead to cracks and electronic leakage during NiO reduction to metallic Ni [24]. These secondary phases are less prevalent at higher temperatures, indicating the potential decomposition and absorption of these phases into BZY grains [31]. However, for samples sintered at 1400 °C EDS analysis revealed the presence of a Y-rich phase, consistent with findings in other studies [22,43,44,47]. Consequently, this experimental setup yields three distinct sample groups, each characterized by a different sintering state, facilitating an investigation into the consequential effects on various material properties.

### 3.3. Effects after $H_2$-reduction of the half-cells

After being heated to 600 °C for 6.5 h and exposed to a reducing atmosphere for 16 h, the electrolyte surfaces of the samples underwent microstructural and structural changes. Fig. 5 shows the XRD patterns of reduced electrolytes after sintering. These diffraction patterns exhibit reflections from the BZY20 primary phase (ICDD database, PDF #04-015-2511), along with additional minor reflections corresponding to secondary phases: Ni-metal (ICDD database, PDF #04–0850), $ZrO_2$ (ICDD database, PDF #00-037-1484), $BaY_2NiO_5$ (ICDD database, PDF #81–1253), and $Y_2O_3$ (ICDD database, PDF #41–1105). Fig. 6 shows the results of the phase quantification of XRD data, and Table S2 summarizes the refined parameters from Rietveld analysis. As previously observed, different percentages of residual secondary phases appear at lower reaction temperatures.

Fig. 7 shows SEM micrographs post-reduction, to be compared to Fig. 4. For samples sintered at 1400 °C and 1325 °C for 10 h, no substantial surface changes were observed. However, small particles with bright contrast emerged on the surfaces of the rest of the samples, which could be identified as metallic Ni, confirming the XRD observations.

The presence of Ni-metal phase on less dense electrolyte surfaces implies the possible decomposition of the pre-existing $BaY_2NiO_5$ phase, resulting in the production of Ni, $Y_2O_3$, and $Ba(OH)_2$ [42]. This may affect the fuel-cell performance [13,41]. These results suggest that the $BaY_2NiO_5$ phase exhibits a transient nature, a conclusion that aligns with findings reported by J. Tong et al. [14], Y. Huang et al. [31], D. Han et al. [42] and W. Deibert et al. [24]. The reduction temperature employed (600 °C) is higher than the Tamman temperature of Ni (581 °C) [15], enhancing Ni diffusion. Additionally, Ni-rich areas in the electrolyte could potentially cause cracks and electronic leakage [24]. The coexistence of Ni-phase, residual $ZrO_2$ phase, and $Y_2O_3$ observed in XRD patterns (Fig. 5) suggest a phenomenon of Ba-loss in the structure of these perovskites.

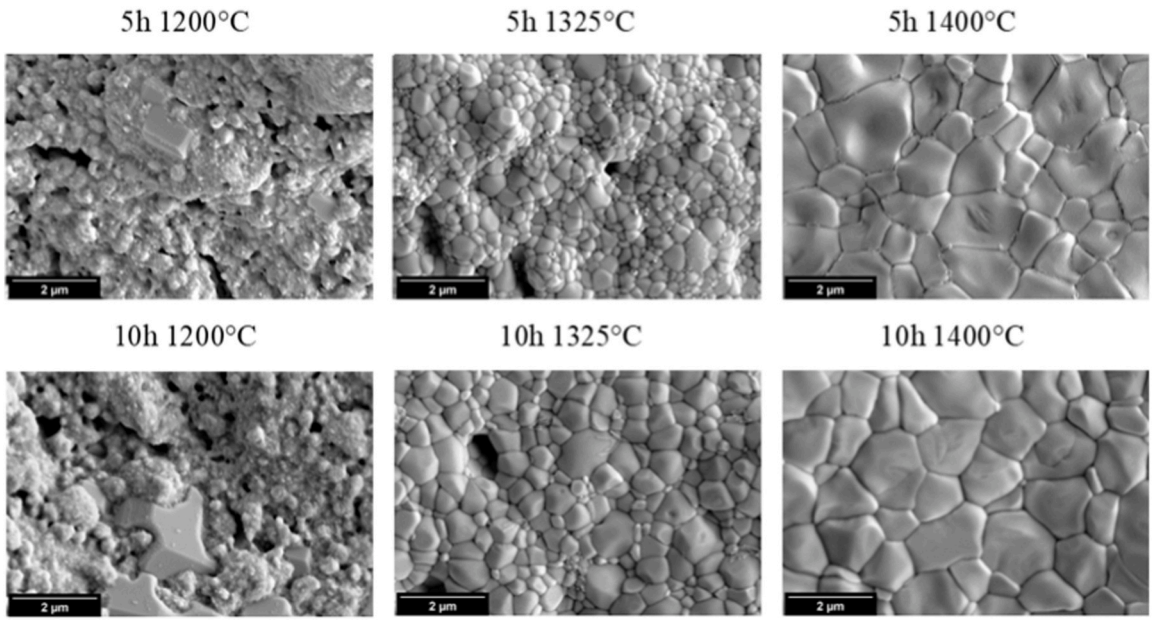


**Fig. 4.** SEM images of sintered BZY20 electrolyte surface under different sintering conditions. The microstructure of the samples differs from the grain formation, grain sizes, and presence of different phases at 1200 °C. Larger and more homogeneous grains appear at sintering temperatures of 1400 °C.

**Table 1**
Morphological parameters of BZY20 sample Surface: grain size (d) and form factor (F). Grain formation is not enough in samples sintered below 1325 °C.

| Sample compound | Sintering conditions | $\bar{d}$ ($\mu m$) | $\bar{F}$ |
|---|---|---|---|
| $BaZr_{0.8}Y_{0.2}O_{3-\delta}$ | 1400 °C 10h | 1.2(6) | 0.74(7) |
| $BaZr_{0.8}Y_{0.2}O_{3-\delta}$ | 1400 °C 5h | 1.3(1.2) | 0.73(7) |
| $BaZr_{0.8}Y_{0.2}O_{3-\delta}$ | 1325 °C 10h | 0.5(3) | 0.8(1) |
| $BaZr_{0.8}Y_{0.2}O_{3-\delta}$ | 1325 °C 5h | 0.3(1) | 0.75(8) |

### 3.4. Residual stress analysis

Considering SEM and XRD findings on the electrolyte side, selecting a sintering temperature of 1400 °C appears prudent for cell fabrication, as it yields proper densification and grain growth of the BZY20 phase without residual phases. However, even with material selection aimed at minimizing thermal mismatch, NiO and Ni's higher thermal expansion coefficients compared to the electrolyte-doped perovskite still induce compression on the electrolyte upon cooling [24,25,48]. For this reason, residual stress measurements were performed on the electrolyte side before and after reduction in a specifically designed diffractometer. The electrolyte layer is about 30 μm (as measured by SEM analysis of a cross-sectioned sample as shown in Fig. S4), which is thick enough to ensure only radiation diffracted at the electrolyte layer reaches the XRD detector. The much larger thickness of the anode (~1.3–1.5 mm) vs the electrolyte (~30 μm) implies that the substrate can be considered semi-infinite for our discussion on residual stresses.

Fig. 8 shows the correlation between residual stresses and sintering temperature. This correlation is shown as a peak shift towards higher angles (2θ) with an increasing tilt angle $\psi$ for the sample sintered at 1400 °C compared to the one sintered at 1200 °C (Fig. 8 (b)). In Fig. 8 (c), the linear regression of strain variation across measured tilt angles is displayed. The sample sintered at 1400 °C for 10 h exhibits greater variation compared to the same sample after reduction, and the sample sintered at 1200 °C for 5 h, which presents smaller variations. Using this fitting and equation (Eq. 3), the residual stresses for each sample are calculated and represented in Fig. 8 (d). As sintering temperature increases, so does stress, an observation that is consistent with increasing densification of the electrolyte (Fig. 4). The measured residual stresses remain relatively stable after the reduction process, except for the sample sintered at 1400 °C for 10 h, which initially exhibited the highest compressive stress. However, this stress decreased after the reduction process (Fig. 8 (d)). It is important to note that this value is an average of three measurements obtained from different points on the sample surface. The stresses measured at different and distant points on the surface did not vary significantly in magnitude, so the electrolyte surface appears to exhibit a homogeneous distribution of stresses.

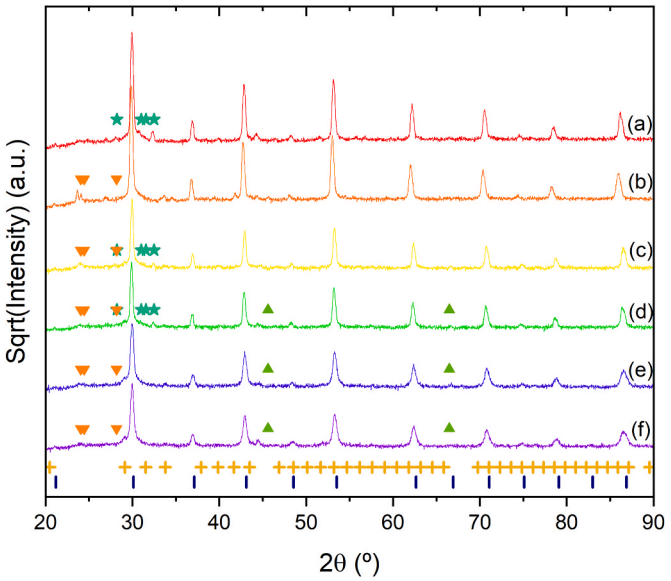


**Fig. 5.** XRD patterns of sintered and reduced electrolytes under different conditions: (a) 1400 °C 10h, (b) 1400 °C 5h, (c) 1325 °C 10h, (d) 1325 °C 5h, (e) 1200 °C 10h, (f) 1200 °C 5h. Sticks (|) indicate the 2θ of XRD peaks of BZY20 according to PDF 04-015-2511. Crosses (+) indicate the 2θ of XRD peaks of $Y_2O_3$ according to PDF 41–1105. Stars (☆) indicate the most significant 2θ of XRD peaks of $BaY_2NiO_5$ according to PDF 81–1253. Triangles (▲) indicate the most significant 2θ of XRD peaks of Ni according to PDF 04–0850. Inverted triangles (▼) indicate the most significant 2θ of XRD peaks of $ZrO_2$ according to PDF 00-037-1484.

According to the results obtained from XRD analysis, the samples

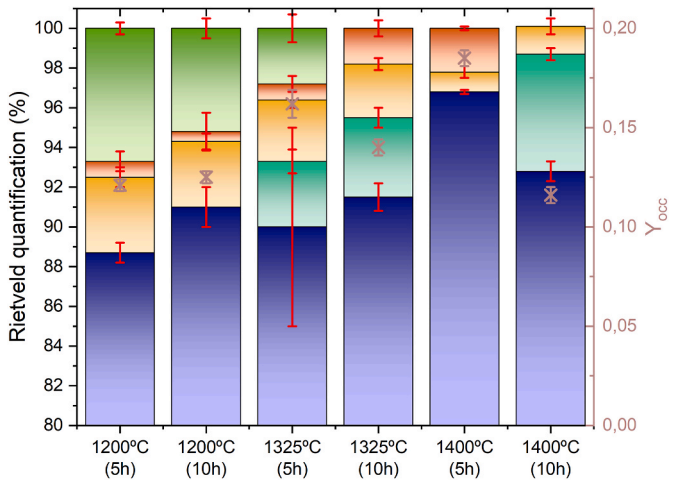


**Fig. 6.** Rietveld quantification of the present phases (Deep blue: BZY20, Aqua: $BaY_2NiO_5$, Gold: $Y_2O_3$, Green: Ni, and Orange: $ZrO_2$) along crosses ( × ) that indicate the Yttrium-occupancy ($Y_{occ}$) in BZY20 structure. $Y_{occ}$ was calculated from the refined lattice parameters by interpolation of literature data. (For interpretation of the references to colour in this figure legend, the reader is referred to the Web version of this article.)

exhibit greater yttrium integration into the structure and fewer residual phases at 1400 °C for 5 h. This favours the conductivity properties of the electrolytes. However, achieving a dense and thin electrolyte layer at higher sintering temperatures, as seen in the SEM images for samples sintered at 1400 °C, comes with the trade-off of generating higher residual stresses in this layer due to differences in the thermal expansion coefficient of the materials in contact and increased densification. Although these residual stresses are mitigated when the anode is reduced, they persist at a significant level in samples sintered at higher temperatures. Notably, these compressive stresses should prevent mechanical failure in the electrolyte [24], but they result in a tensile stress on the anode, potentially leading to delamination. The relaxation of stresses shown in Fig. 8 (d) can cause cracks and defects that worsen with thermal cycling. The presence of stresses in the electrolyte underscores the importance of achieving a good match between the contacting components for the long-term durability of the cell [27–29]. While these stresses may not have catastrophic implications at laboratory scale, their impact may be substantial in larger industrial-scale fuel cell stacks.

## 4. Conclusion

Sintering at higher temperatures (1400 °C) with shorter soaking times is a promising approach for obtaining well-formed BZY20 electrolyte layers with larger grain sizes that enhance the mechanical and electrical properties of the electrolyte for improved fuel cell performance.

There are however challenges, including the presence of impurities such as $Y_2O_3$ and $BaY_2NiO_5$, particularly at lower sintering temperatures, which can negatively affect fuel cell performance and long-term stability. Addressing this issue requires minimizing impurity formation and optimising the anode reduction process to prevent Ni-rich areas that could lead to cracks and electronic leakage. Additionally, residual stresses resulting from thermal mismatch between the anode and electrolyte can impact cell durability. While compressive stresses on the electrolyte's surface may offer some mechanical stability benefits, they can lead to tensional stresses on the anode, causing defects as it has been previously seen. Thus, careful consideration of material compatibility and sintering conditions is essential to ensure an adequate stress distribution across fuel cell components. The objective of establishing a correlation between six different sintering points with the structural formation of a BZY20-based electrolyte layer and residual stresses is achieved, emphasizing the measurement of these stresses and their importance for future studies. Overall, this research provides valuable insights into fabricating BZY20 electrolytes for anode-supported PCFCs facilitating further optimization of the sintering process and materials integration steps to enhance overall performance and long-term stability.

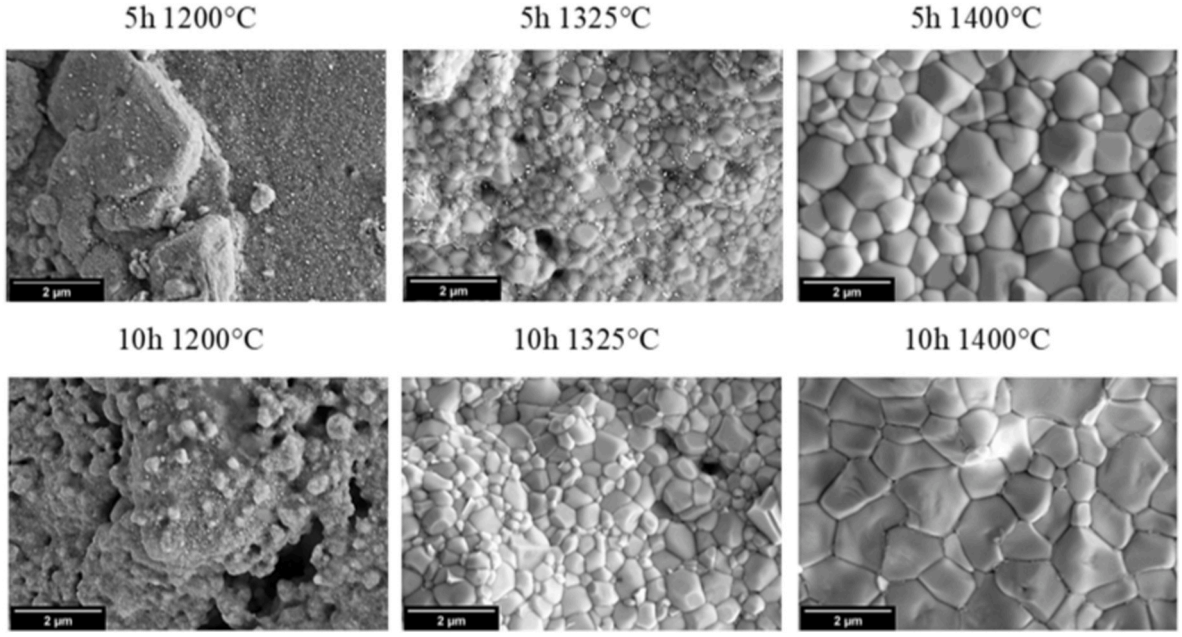


**Fig. 7.** SEM images of sintered and reduced BZY20 electrolyte surface under different sintering conditions. The microstructure of the samples differs from the grain formation, grain sizes, and presence of different phases. Bright small particles of Ni appeared at 1200 °C and 1325 °C. Larger and more homogeneous grains appear at sintering temperatures of 1400 °C.

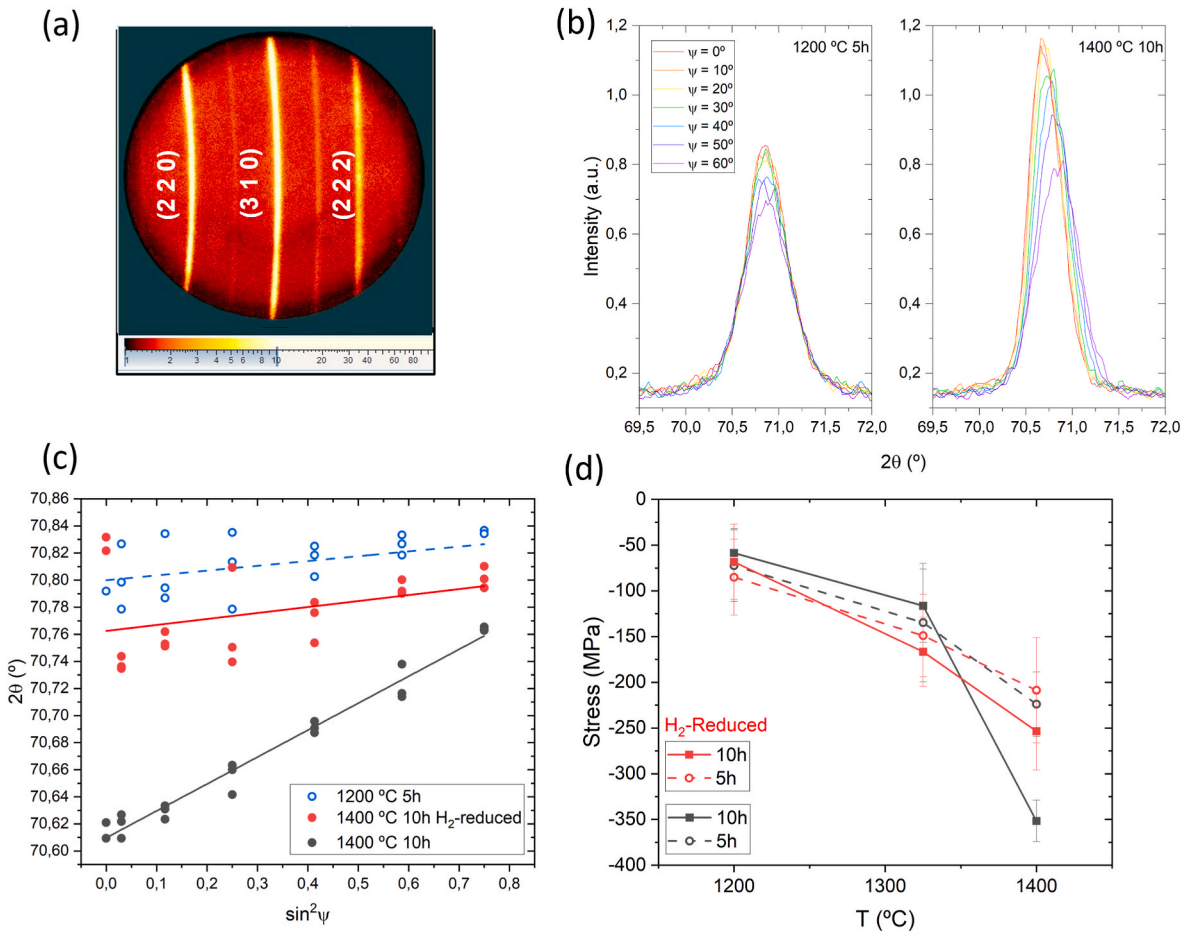


**Fig. 8.** Residual stress measurement results. (a) Frame from the area detector showing traces of the Debye rings from BZY20. (b) Integrated peaks from (3 1 0) reflections of the samples sintered at 1200 °C for 5 h (left) and sintered at 1400 °C for 10h (right) at different tilt angles. (c) 2θ vs. $sin^2\ \psi$ variation and their corresponding linear fit for the samples sintered at 1200 °C for 5 h (○) and sintered at 1400 °C for 10 h (●). (d) Variation of residual stress as a function of sintering temperature. Continuous line groups the samples sintered for 10h (■) and the dash-line groups the samples sintered for 5h (□).

## CRediT authorship contribution statement

**Sol Fernández Muñoz:** Data curation, Investigation, Methodology, Visualization, Writing – original draft. **Ricardo Chacartegui:** Conceptualization, Funding acquisition, Methodology, Supervision, Validation, Writing – review & editing. **María D. Alba:** Data curation, Investigation, Methodology, Validation, Writing – review & editing. **Joaquín Ramírez Rico:** Conceptualization, Data curation, Funding acquisition, Project administration, Resources, Supervision, Validation, Writing – review & editing.

## Declaration of competing interest

The authors declare that they have no known competing financial interests or personal relationships that could have appeared to influence the work reported in this paper.

## Data availability

Data will be made available on request.

## Acknowledgements

This work was funded by the Spanish Ministry of Science and Innovation under Grant no. PID2019-107019RB-I00 (co-financed with FEDER funds).

## Appendix A. Supplementary data

Supplementary data to this article can be found online at https://doi.org/10.1016/j.jpowsour.2024.234070.

## References

[1] E.P. Murray, T. Tsai, S.A. Barnett, A Direct-Methane Fuel Cell with a Ceria-Based Anode, Nature 400 (1999) 649–651, https://doi.org/10.1038/23220.
[2] L.P. Putilov, A.K. Demin, V.I. Tsidilkovski, P. Tsiakaras, Theoretical modeling of the gas humidification effect on the characteristics of proton ceramic fuel cells, Appl. Energy 242 (2019) 1448–1459, https://doi.org/10.1016/j.apenergy.2019.03.096.
[3] S. Park, J.M. Vohs, R.J. Gorte, Direct Oxidation of Hydrocarbons in a Solid-Oxide Fuel Cell, Nature 404 (2000) 265–267, doi: 10.1038/35005040.
[4] M.S. Takashi Hibino, Atsuko Hashimoto, Inoune Takao, Jun-ichi Tokuno, S. I. Yoshida, A Low-Operating-Temperature Solid Oxide Fuel Cell in Hydrocarbon-Air Mixtures, Science 288 (2000) 2031–2033, https://doi.org/10.1126/science.288.5473.2031.
[5] E. Fabbri, D. Pergolesi, E. Traversa, Materials challenges toward proton-conducting oxide fuel cells: a critical review, Chem. Soc. Rev. 39 (11) (2010) 4355–4369, https://doi.org/10.1039/b902343g.
[6] A.J. Jacobson, Materials for Solid Oxide Fuel Cells, Chem. Mater. 22 (2010) 660–674, https://doi.org/10.1021/cm902640j.
[7] K.D. Kreuer, S. Adams, W. Münch, A. Fuchs, U. Klock, J. Maier, Proton conducting alkaline earth zirconates and titanates for high drain electrochemical applications, Solid State Ionics 145 (1–4) (2001) 295–306, https://doi.org/10.1016/S0167-2738(01)00953-5.
[8] K.D. Kreuer, Aspects of the formation and mobility of protonic charge carriers, Solid State Ionics 125 (1999) 285–302, https://doi.org/10.1016/S0167-2738(99)00188-5.

[9] L. Bi, S.P. Shafi, E. Traversa, Y-doped $BaZrO_3$ as a chemically stable electrolyte for proton-conducting solid oxide electrolysis cells (SOECs), J Mater Chem A Mater 3 (11) (Mar. 2015) 5815–5819, https://doi.org/10.1039/c4ta07202b.

[10] P.I. Cowin, C.T.G. Petit, R. Lan, J.T.S. Irvine, S. Tao, Recent Progress in the Development of Anode Materials for Solid Oxide Fuel Cells, Advanced Energy Materials 1 (3) (2011) 314–332, https://doi.org/10.1002/aenm.201100108.

[11] E. Fabbri, L. Bi, D. Pergolesi, E. Traversa, Towards the next generation of solid oxide fuel cells operating below 600 °C with chemically stable proton-conducting electrolytes, Adv. Mater. 24 (2) (2012) 195–208, https://doi.org/10.1002/adma.201103102.

[12] Á. Triviño-Peláez, D. Pérez-Coll, J. Mosa, G.C. Mather, M. Aparicio, D.P. Fagg, Processing and characterisation of $BaZr_{0.8}Y_{0.2}O_3$ proton conductor densified at 1200°C, J Mater Chem A Mater (2022) 4428, https://doi.org/10.1039/d1ta09998a. –4439.

[13] J. Tong, D. Clark, M. Hoban, R.O. Hayre, Cost-effective solid-state reactive sintering method for high conductivity proton conducting yttrium-doped barium zirconium ceramics, Solid State Ionics 181 (11–12) (2010) 496–503, https://doi.org/10.1016/j.ssi.2010.02.008.

[14] J. Tong, D. Clark, L. Bernau, M. Sanders, R. O'Hayre, Solid-state reactive sintering mechanism for large-grained yttrium-doped barium zirconate proton conducting ceramics, J. Mater. Chem. 20 (30) (2010) 6333–6341, https://doi.org/10.1039/c0jm00381f.

[15] C. Duan, "Ceramic electrochemical cells for power generation and fuel production," Phd Thesis, Colorado School of Mines, Golden, 2019.

[16] C. Duan, et al., Highly efficient reversible protonic ceramic electrochemical cells for power generation and fuel production, Nat. Energy 4 (3) (Mar. 2019) 230–240, doi:10.1038/s41560-019-0333-2.

[17] S. Nikodemski, J. Tong, R. O'Hayre, Solid-state reactive sintering mechanism for proton conducting ceramics, Solid State Ionics 253 (2013) 201–210, https://doi.org/10.1016/j.ssi.2013.09.025.

[18] B.C.H. Steele, A. Heinzel, Materials for fuel-cell technologies, Nature 414 (2001) 345–352, https://doi.org/10.1038/35104620.

[19] D. Han, N. Hatada, T. Uda, R. Koc, Chemical expansion of yttrium-doped barium zirconate and correlation with proton concentration and conductivity, J. Am. Ceram. Soc. 99 (11) (2016) 3745–3753, https://doi.org/10.1111/jace.14377.

[20] D. Han, T. Uda, The best composition of an Y-doped $BaZrO_3$ electrolyte: selection criteria from transport properties, microstructure, and phase behavior, J Mater Chem A Mater 6 (38) (2018) 18571–18582, https://doi.org/10.1039/c8ta06280c.

[21] J. Li, C. Wang, X. Wang, L. Bi, Sintering aids for proton-conducting oxides – a double-edged sword? A mini review, Electrochem. Comm 112 (2020), https://doi.org/10.1016/j.elecom.2020.106672.

[22] Y. Yamazaki, R. Hernandez-Sanchez, S.M. Haile, Cation non-stoichiometry in yttrium-doped barium zirconate: phase behavior, microstructure, and proton conductivity, J. Mater. Chem. 20 (37) (2010) 8158–8166, https://doi.org/10.1039/c0jm02013c.

[23] C. Duan, J. Tong, M. Shang, M. Sanders, S. Ricote, R.O. Hayre, Readily Processed Protonic Ceramic Fuel Cells with High Performance at Low Temperatures, Science 349 (2015) 1321–1326, https://doi.org/10.1126/science.aab3987.

[24] W. Deibert, M.E. Ivanova, Y. Huang, R. Merkle, Fabrication of multi-layered structures for proton conducting ceramic cells, J. Mater. Chem. A 3 (2022) 2362–2373, https://doi.org/10.1039/d1ta05240c.

[25] A. Løken, S. Ricote, S. Wachowski, Thermal and chemical expansion in proton ceramic electrolytes and compatible electrodes, Crystals 8 (2018) 9, https://doi.org/10.3390/cryst8090365.

[26] D. Han, K. Shinoda, T. Uda, Dopant site occupancy and chemical expansion in rare earth-doped barium Zirconate, J. Am. Ceram. Soc. 97 (2) (2014) 643–650, https://doi.org/10.1111/jace.12681.

[27] T. Horita, Y. Xiong, H. Kishimoto, K. Yamaji, N. Sakai, H. Yokokawa, Application of Fe – Cr Alloys to Solid Oxide Fuel Cells for Cost-Reduction Oxidation Behavior of Alloys in Methane Fuel, Journal of Power Sources 131 (2004) 293–298, https://doi.org/10.1016/j.jpowsour.2003.10.017.

[28] F. Jtilich, D. Jtilich, Thermal Expansion of SOFC Materials, Ionics 5 (1999) 129–139, doi: 10.1007/BF02375916.

[29] K. Park, S. Yu, J. Bae, H. Kim, Y. Ko, Fast performance degradation of SOFC caused by cathode delamination in long-term testing, Int. J. Hydrogen Energy 35 (16) (2010) 8670–8677, https://doi.org/10.1016/j.ijhydene.2010.05.005.

[30] S. Choi, et al., Exceptional power density and stability at intermediate temperatures in protonic ceramic fuel cells, Nat. Energy 3 (3) (2018) 202–210, https://doi.org/10.1038/s41560-017-0085-9.

[31] Y. Huang, R. Merkle, J. Maier, Effects of NiO addition on sintering and proton uptake of Ba(Zr,Ce,Y)O3-d, Mater. Chem. 9 (2021) 14775–14785, https://doi.org/10.1039/D1TA02555D.

[32] H. Shimada, et al., A key for achieving higher open-circuit voltage in protonic ceramic fuel cells: lowering interfacial electrode polarization, ACS Appl. Energy Mater. 2 (1) (2019) 587–597, https://doi.org/10.1021/acsaem.8b01617.

[33] A. Le Bail, H. Duroy, J.L. Fourquet, Ab-initio structure determination of LiSbWO6 by X-ray powder diffraction, Mater. Res. Bull. 23 (1988) 447–452, https://doi.org/10.1016/0025-5408(88)90019-0.

[34] M.D. Gonçalves, P.S. Maram, R. Muccillo, A. Navrotsky, Enthalpy of formation and thermodynamic insights into yttrium doped BaZrO 3, J. Mater. Chem. A: Materials for energy and sustainability 2 (2014) 17840–17847, https://doi.org/10.1039/C4TA03487B.

[35] P.S. Prevey, X-Ray Diffraction Residual Stress Techniques, Mater Charact (1986) 380–392, https://doi.org/10.31399/asm.hb.v10.a0001761.

[36] V. Hauk, Structural and Residual Stress Analysis by Nondestructive Methods, Elsevier Science B. V. 4 (1) (1997), doi:10.1016/B978-0-444-82476-9.50022-0.

[37] M.E. Fitzpatrick, A.T. Fry, P. Holdway, F.A. Kandil, J. Shackleton, L. Souminen, "NPL Good Practice Guide no . 52 : determination of residual stresses by x-ray diffraction Determination of Residual Stresses by X-ray, Diffraction - Issue 2 (52) (2002) 9–11.

[38] S.Y. Lee, J. Ling, S. Wang, J. Ramirez-Rico, Precision and accuracy of stress measurement with a portable X-ray machine using an area detector, J. Appl. Crystallogr. 50 (1) (2017) 131–144, https://doi.org/10.1107/S1600576716018914.

[39] I.C. Noyan, J.B. Cohen, An X-ray diffraction study of the residual stress-strain distributions in shot-peened two-phase brass, Mater. Sci. Eng. 75 (1–2) (1985) 179–193, https://doi.org/10.1016/0025-5416(85)90188-0.

[40] J. Ramirez-Rico, S.Y. Lee, J.J. Ling, I.C. Noyan, Stress measurement using area detectors: a theoretical and experimental comparison of different methods in ferritic steel using a portable X-ray apparatus, J. Mater. Sci. 51 (11) (2016) 5343–5355, https://doi.org/10.1007/s10853-016-9837-3.

[41] F. Iguchi, K. Hinata, High-temperature elastic properties of yttrium-doped zirconate, Metals 11 (2021) 968, https://doi.org/10.3390/met11060968.

[42] D. Han, Y. Otani, Y. Noda, T. Onishi, M. Majima, T. Uda, Strategy to improve phase compability between proton conductive $BaZr_{0.8}Y_{0.2}O_3$ and nickel oxide, RSC Adv. (2016), https://doi.org/10.1039/C5RA26947D.

[43] Y. Huang, R. Merkle, J. Maier, Effect of NiO addition on proton uptake of $BaZr_{1-x}Y_xO_{3-x/2}$ and $BaZr_{1-x}Sc_xO_{3-x/2}$ electrolytes, Solid State Ionics 347 (2020), https://doi.org/10.1016/j.ssi.2020.115256.

[44] D. Han, K. Kishida, K. Shinoda, H. Inui, T. Uda, A comprehensive understanding of structure and site occupancy of Y in Y-doped $BaZrO_3$, J Mater Chem A (9) (2013) 3027–3033, https://doi.org/10.1039/c2ta00675h.

[45] A. Magrez, T. Schober, Preparation, sintering, and water incorporation of proton conducting $Ba_{0.99}Zr_{0.8}Y_{0.2}O_{3-\delta}$: comparison between three different synthesis techniques, Solid State Ionics 175 (1–4) (2004) 585–588, https://doi.org/10.1016/j.ssi.2004.03.045.

[46] E. Makagon, R. Merkle, J. Maier, I. Lubomirsky, Influence of Hydration and Dopant Ionic Radius on the Elastic Properties of BaZrO3, Solid State Ionics 344 (2019), https://doi.org/10.1016/j.ssi.2019.115130.

[47] J. Tong, D. Clark, L. Bernau, A. Subramaniyan, R. O'Hayre, Proton-conducting yttrium-doped barium cerate ceramics synthesized by a cost-effective solid-state reactive sintering method, Solid State Ionics 181 (33–34) (2010) 1486–1498, https://doi.org/10.1016/j.ssi.2010.08.022.

[48] L.P. Wendler, K. Ramos, D.M.P.F. Souza, Investigation about the reason of limited grain growth of Y-doped barium zirconate, Ceram. Int. 45 (15) (2019) 19120–19126, https://doi.org/10.1016/j.ceramint.2019.06.158.